

Supplementary Material for: Observation of stimulated Brillouin scattering in silicon nitride integrated waveguides

Flavien Gyger^{1,*}, Junqiu Liu^{2,*}, Fan Yang^{1,*}, Jijun He², Arslan S. Raja²,
Rui Ning Wang², Sunil A. Bhave³, Tobias J. Kippenberg², and Luc Thévenaz¹

* These authors contributed equally to this work.

¹Group for Fibre Optics, Swiss Federal Institute of Technology Lausanne (EPFL), CH-1015
Lausanne, Switzerland

²Laboratory of Photonics and Quantum Measurements, Swiss Federal Institute of
Technology Lausanne (EPFL), CH-1015 Lausanne, Switzerland

³OxideMEMS Lab, Purdue University, 47907 West Lafayette, IN, USA

Contents

S1	Challenges, quantitative arguments	S1
S1.1	Noise induced by polarization and temperature fluctuations	S1
S1.2	Pump reflection	S2
S1.3	Cavity Kerr effect	S2
S1.4	Stimulated Raman scattering	S3
S2	Sample fabrication	S4
S3	Simulations	S4
S4	Detailed experimental setup	S5
S5	Detailed gain calculation	S5
S5.1	System response	S5
S5.2	Gain calculation	S7
S5.3	Error bar estimation	S7
S6	Threshold calculation	S7

S1 Challenges, quantitative arguments

In our waveguide, the silicon nitride (Si_3N_4) Brillouin gain has been measured to be $g_B = 8 \times 10^{-14}$ m/W ($g_B/A_{\text{eff}} = 0.07$ m⁻¹W⁻¹, where $A_{\text{eff}} = 1.2$ μm^2 is the effective area). Thus, the probe beam, just after coming out of the waveguide, has a Brillouin-induced maximum intensity variation of the order of:

$$G_B \approx \frac{g_B}{A_{\text{eff}}} P_{P0} L \sqrt{\alpha_{\text{wg}}} \approx 1.6 \times 10^{-5}, \quad (1)$$

where $P_{P0} \approx 100$ mW is the pump power inside the waveguide, $\alpha_{\text{wg}} \approx 0.2$ (7 dB) is the waveguide insertion loss and $L \approx 5$ mm is the waveguide's length. For example, considering a detected probe power of 0 dBm, the probe power resulting from stimulated Brillouin scattering (SBS) at the gain peak is at -48 dBm. As a consequence, any superimposed fluctuation with a standard deviation exceeding this value will inevitably screen the Brillouin signal. We now proceed to quantitatively describe the sources of noise sources faced in the experiments.

S1.1 Noise induced by polarization and temperature fluctuations

When a continuous wave (CW) pump-probe setup is used, such as the one presented in Fig. S1(a), the measured probe power presents large fluctuations. A typical representation of this noise is given in Fig. S1(b). Each acquisition leads to a random trace waveform similar to the one shown. This noise is generated by random thermal/polarization fluctuations modulating the fraction of pump power being coupled into the cavity, which in turn dictates the waveguide's temperature. These fluctuations modulate the probe transmission and the resulting substantial probe variation (with a standard deviation approximately equal to 20 % of the mean value) compared to the small gain value to be measured prevents any CW experiment to be conclusive in measuring the Brillouin gain.

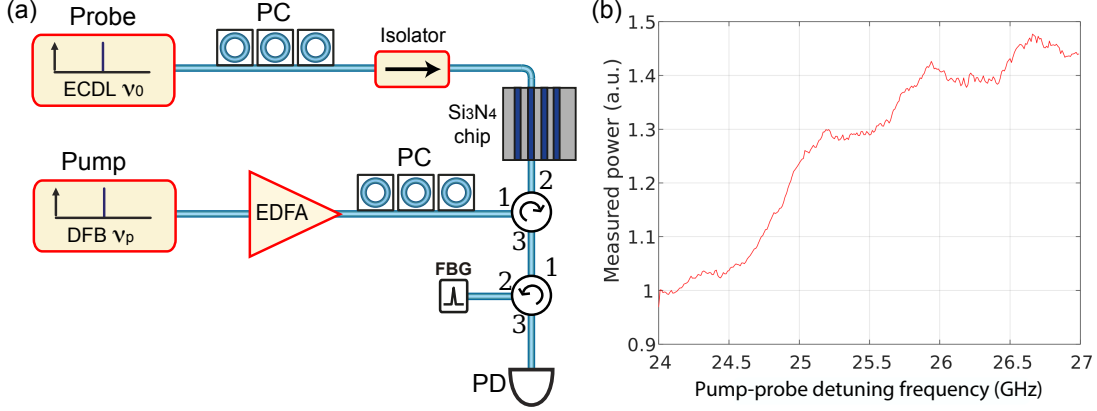


Figure S1: **CW pump-probe experiment.** (a) Experimental setup. (b) Measured signal showing large fluctuations. ECDL, external-cavity diode laser; PC, polarization controller; EDFA, erbium-doped fiber amplifier; DFB laser, distributed feedback laser; FBG, fiber Bragg grating; PD, photodetector.

S1.2 Pump reflection

Power reflection from the chip coupling points is experimentally measured to be $R_{wg} \approx -22$ dB. This means that 0.5% of the pump power returns back and directly hits the detector in the absence of optical filtering. On top of the risk of damaging the detector when using high pump powers (e.g. 1 W), the noise induced by this reflection totally screens the Brillouin gain signal. Thus, the pump beam needs to be optically filtered out from the probe using fiber Bragg gratings (FBGs). In the triple intensity modulation setup, we further filtered out the pump signal in the radio-frequency (RF) domain by modulating both pump and probe beams at a slightly different frequency and detecting the signal at the frequency difference, as explained in the main manuscript. This filtering method is very effective and totally suppresses the impact of the pumps on the measurement signal.

S1.3 Cavity Kerr effect

Probe modulation by Kerr phase-to-intensity conversion induced by an intensity-modulated pump is depicted in Fig. S2. We now calculate the probe modulation amplitude in the worst case scenario (which occurs at random times due to random temperature/polarization fluctuations). The waveguide-induced cavity free spectral range (FSR) is:

$$\nu_F \approx \frac{c}{2n_g L}, \quad (2)$$

where $n_g = 2.1$ is the group refractive index at 1550 nm wavelength, c is the speed of light in vacuum and L is the waveguide length. The change in FSR due to Kerr effect as a function of the pump power is:

$$\frac{\partial \nu_F}{\partial P} \approx -\frac{c}{2n_g^2 L} \frac{\partial n_g}{\partial P}, \quad (3)$$

for which

$$\frac{\partial n_g}{\partial P} = \frac{\partial n}{\partial P} = \frac{n_2}{A_{\text{eff}}}, \quad (4)$$

where $n_2 = 2.5 \times 10^{-19} \text{ m}^2 \text{W}^{-1}$ is the Si_3N_4 Kerr coefficient [1] and $A_{\text{eff}} = 1.2 \text{ } \mu\text{m}^2$ is the waveguide's effective area. The FSR change is given by:

$$\Delta \nu_{F,\text{MAX}} = \frac{\partial \nu_F}{\partial P} \Delta P = -\frac{n_2 c}{2n_g^2 L A_{\text{eff}}} \Delta P \approx -283 \text{ Hz}, \quad (5)$$

where ΔP is the total power variation of the pump beam. In our case, $\Delta P = 200 \text{ mW}$. So the maximum cavity spectrum shift at the optical frequency ν_0 is:

$$m \cdot |\Delta \nu_{F,\text{MAX}}| \approx 4 \text{ MHz}, \quad (6)$$

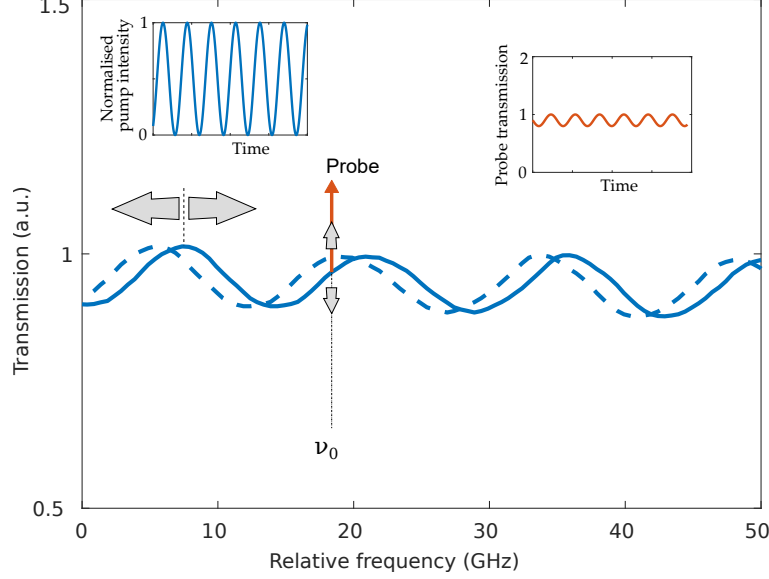


Figure S2: **Illustration of Kerr modulation.** An intensity-modulated pump periodically shifts the probe transmission spectrum, which in turns modulates the probe signal at the pump frequency. The solid blue trace corresponds to the measured waveguide transmission spectrum as a function of a relative frequency starting at 193.5 THz. The dotted line represents this same spectrum shifted in frequency by pump-induced Kerr effect. Note that the shift is exaggerated for clarity.

where $m = \nu_0/\nu_F \approx 13535$ is the number of resonances from DC to ν_0 . Now, we calculate the transmission spectrum variation for the probe. The waveguide's induced cavity transmission spectrum can be expressed as [2]:

$$P_N = \frac{1}{1 + \left(2\frac{F}{\pi}\right)^2 \sin^2\left(\pi\frac{\nu}{\nu_F}\right)}, \quad (7)$$

where P_N is the normalized transmitted power and F is the cavity finesse. In our case, $\nu_F = 14.375$ GHz. Since the finesse is low, it can be simplified to:

$$P_N \approx 1 - 2\frac{F^2}{\pi^2} + 2\frac{F^2}{\pi^2} \cos\left(2\pi\frac{\nu}{\nu_F}\right). \quad (8)$$

Referring to the measured transmission spectrum shown in Fig. 2(a) of the main manuscript, the finesse can be found to be: $F \approx 0.53$. The maximum slope of Eq. (8) is:

$$S_{\text{MAX}} = \max_{\nu} \left\{ \frac{\partial P_N}{\partial \nu} \right\} = \frac{4F^2}{\pi\nu_F}. \quad (9)$$

In our case, we have $S_{\text{MAX}} \approx 24.9 \text{ THz}^{-1}$. Combining this last result with Eq. (6), we obtain a worst-case probe variation of $G_K \approx 10^{-4}$, which is more than six times higher than the targeted Brillouin signal of Eq. (1). In an idealized situation, this generated signal should be constant and only contribute as an offset. However, the cavity spectrum randomly shifts due to fluctuations of temperature and of pump coupling rate into the waveguide. In turn, these shifts result in random variations of the offset, with a standard deviation two times larger than the peak Brillouin gain.

S1.4 Stimulated Raman scattering

At a pump-probe detuning frequency equal to the Brillouin frequency shift, $\Delta\nu = \nu_B = 25$ GHz, the silica Raman gain can be estimated to be [3]:

$$g_R(\nu_B) \approx g_{R,\text{MAX}} \cdot 1.8 \times 10^{-3} \approx 10^{-16} \text{ m/W}, \quad (10)$$

where $g_{R,\text{MAX}} = 6.5 \times 10^{-14}$ m/W is the peak silica Raman gain. Our patchcord length connecting to the waveguide is $L_{\text{pc}} = 1$ m for each side. Given that the chip insertion loss is $\alpha_{\text{wg}} \approx 0.2$ (7 dB) and by taking into account the two coupling patchcords as well as the 1-cm-long high numerical aperture (NA) fibers used to couple the light into the waveguide, the total effective length is: $L_{\text{pc,eff}} \approx 2.4$ m.

Taking patchcord's effective area to be $A_{\text{eff,SMF}} \approx 80 \mu\text{m}^2$ and considering that the pump power inside the patchcord is $P_{P1,\text{SMF}} = 24$ dBm, the total stimulated Raman scattering generated along in the patchcords is:

$$G_R \approx \frac{g_R(\nu_B)}{A_{\text{eff,SMF}}} \cdot L_{\text{pc,eff}} \cdot P_{P1,\text{SMF}} \approx 10^{-6}. \quad (11)$$

Hence, in the present case, this background signal is smaller than the peak Brillouin signal and, despite contributing to the total system uncertainty, its fluctuations do not exceed the Si_3N_4 peak Brillouin gain. Nonetheless, it is reduced thanks to the use of the triple intensity modulation experimental setup, as described in the main manuscript.

S2 Sample fabrication

The integrated low-loss Si_3N_4 waveguides are fully buried in a SiO_2 cladding. The Si_3N_4 waveguide sample presented in this work is fabricated using the subtractive process [4, 5]. In this process, the Si_3N_4 film from low-pressure chemical vapour deposition (LPCVD) is first deposited on the thermal wet oxide substrate on a 4-inch silicon wafer. Electron beam lithography (EBL) is used to pattern the waveguides, followed by dry etching using CHF_3/O_2 gases which transfers the waveguide pattern from the EBL resist mask (HSQ) to the SiO_2 substrate. Afterwards, the entire wafer is annealed at 1200°C to drive out the residual hydrogen content [6] in Si_3N_4 which can cause strong light absorption losses. Top SiO_2 cladding of $2.3 \mu\text{m}$ thickness is then deposited on the substrate, followed by SiO_2 thermal annealing at 1200°C once again. Due to the added height of the waveguide before SiO_2 cladding deposition, a dome-shaped top silica-air boundary is formed (i.e. with self-alignment) after deposition, as shown in the simulation results of Fig. 3 of the main manuscript. Finally, the wafer is separated into chips of $5 \times 5 \text{ mm}^2$ in size via dicing or deep dry etching.

Inverse nanopapers are used to couple light both into and out of the chip via high numerical aperture (NA) fibers [7]. The coupling loss is less than 2 dB/facet, corresponding to a fiber-chip-fiber through coupling efficiency of 40%. The high NA fibers are packaged to the Si_3N_4 chip [8], which allow compact, portable devices for transfer and easy integration into a fiber system.

Concerning the dimension variation of the sample: The long-range variation of the mean value of Si_3N_4 waveguide height is within ± 1 nm range for the 5-mm-long waveguide, calculated based on the standard LPCVD Si_3N_4 process with $<1\%$ deposition non-uniformity over a 4-inch wafer scale. This long-range variation value of waveguide height is comparable to the short-range surface roughness of as-deposited Si_3N_4 film. The waveguide was patterned using electron beam lithography (EBL) using optimized exposure dose and beam size with electron proximity effect correction. The waveguide width variation (i.e. line edge roughness, LER) is within ± 3 nm, analyzed using a professional software ProSEM. Similarly, the bottom SiO_2 cladding, grown from thermal wet oxidation of silicon, has $<0.1\%$ non-uniformity over the 4-inch wafer scale; The top SiO_2 cladding, deposited via LPCVD low-temperature oxide (LTO) process, has $<2\%$ non-uniformity over the 4-inch wafer scale. Therefore, the calculated long-range variation of the mean SiO_2 thickness is within ± 4 nm range for the 5-mm-long waveguide.

S3 Simulations

Simulations of the optical and acoustic modes are performed using COMSOL® 2D "Electromagnetic Waves, Frequency Model" and 3D "Solid Mechanics" modules, respectively. Si_3N_4 refractive index $n_{\text{Si}_3\text{N}_4} = 2.00$ and SiO_2 refractive index $n_{\text{SiO}_2} = 1.45$ are used to compute the optical modes. Si_3N_4 density $\rho_{\text{Si}_3\text{N}_4} = 3100 \text{ kg/m}^3$, Si_3N_4 Young's modulus $E_{\text{Si}_3\text{N}_4} = 280 \text{ GPa}$ [9], SiO_2 density $\rho_{\text{SiO}_2} = 2203 \text{ kg/m}^3$ and SiO_2 Young's modulus $E_{\text{SiO}_2} = 73 \text{ GPa}$ are used to compute the acoustic eigenmodes. These acoustic eigenmodes are computed by solving the equation of motion in frequency domain, including the strain-displacement relation and Hooke's law. For each acoustic eigenmode, the Brillouin gain is obtained by computing the overlap integral between the eigenmode displacement field and the body forces resulting from the divergence of the

electrostrictive (stress) tensor [10]. Acoustic phonon leakage and subsequent reflections at the chip upper part (SiO_2) and at the silicon substrate are taken into account by including the SiO_2 cladding, the silicon substrate and a surrounding $1.5\ \mu\text{m}$ thick PML in the simulation (except for the upper part for which a free boundary is used to imitate the silica-air boundary). The acoustic damping is calculated from the measured Brillouin linewidth of 390 MHz. The Si_3N_4 photoelastic constant p_{12} is adjusted to match the Brillouin gain obtained from our simulations to the measurement data (see the discussion section in the main manuscript). The simulation results are slightly shifted in frequency (220 MHz) to match the measurement results. This shift probably results from a slight mismatch of parameters in the simulation, such as Young's modulus or density.

S4 Detailed experimental setup

The detailed experimental setup is shown in Fig. S3. The intensity modulators are Mach-Zehnder modulators with their bias set at the quadrature point, as shown in the inset of Fig. S3. The two pumps are coupled via an asymmetrical coupler having a higher coupling rate for the second pump. Perfect matching of the two pumps intensity is then achieved by precise tuning of a variable attenuator on the second pump path. Perfect polarization matching is realized by placing a polarizer on the pump common path, thereby forcing the two beams to have the same polarization state. The frequency offset of the two pump beams is controlled by the temperature controllers of the two distributed feedback lasers. The long-term accuracy of the frequency offset of the two pump beams is within a few tens of MHz, which has negligible effect on the background noise because it is much smaller than the cavity free spectral range (i.e. 14.375 GHz). The time evolution of the total pump intensity is monitored in real time before entering and after exiting the chip, ensuring an optimum intensity cancellation during the whole scanning procedure. In the case of an imperfect cancellation due to unbalanced intensity of the two pump beams, the fluctuating background increases to values above $1\ \mu\text{V}$ and, most of the time, fully covers the Brillouin signal.

S5 Detailed gain calculation

S5.1 System response

The system response of the experimental setup presented in Fig. S3 and its derivation are briefly described. In this derivation, only one pump (i.e. pump1) is considered, as the second one (i.e. pump2) does not contribute to the stimulated Brillouin scattering interaction.

Mach-Zehnder modulator

We first derive the response of a lossless Mach-Zehnder modulator assuming that it is driven with the following sinusoidal RF signal:

$$V(t) = \frac{2}{\pi} \varsigma V_\pi \sin(\Omega t), \quad (12)$$

where $V(t)$ is the applied voltage, ς represents the modulation depth, V_π is the modulator's pi voltage and $\Omega/2\pi$ is the applied RF frequency. The output optical power at the output of a Mach-Zehnder modulator, having its bias set in the quadrature point, can be shown to be:

$$P(t) = P_0 \left(1 - \sum_n J_n(2\varsigma_P) \sin(n\Omega t) \right), \quad (13)$$

where P_0 is the input optical power and J_n are the modified Bessel functions of the first kind of n -th order.

Stimulated Brillouin scattering

Evolution of the probe electric field envelope co-propagating along the z -axis, $E_s(z)$, in presence of stimulated Brillouin scattering in the Si_3N_4 , is governed by the following differential equation [11]:

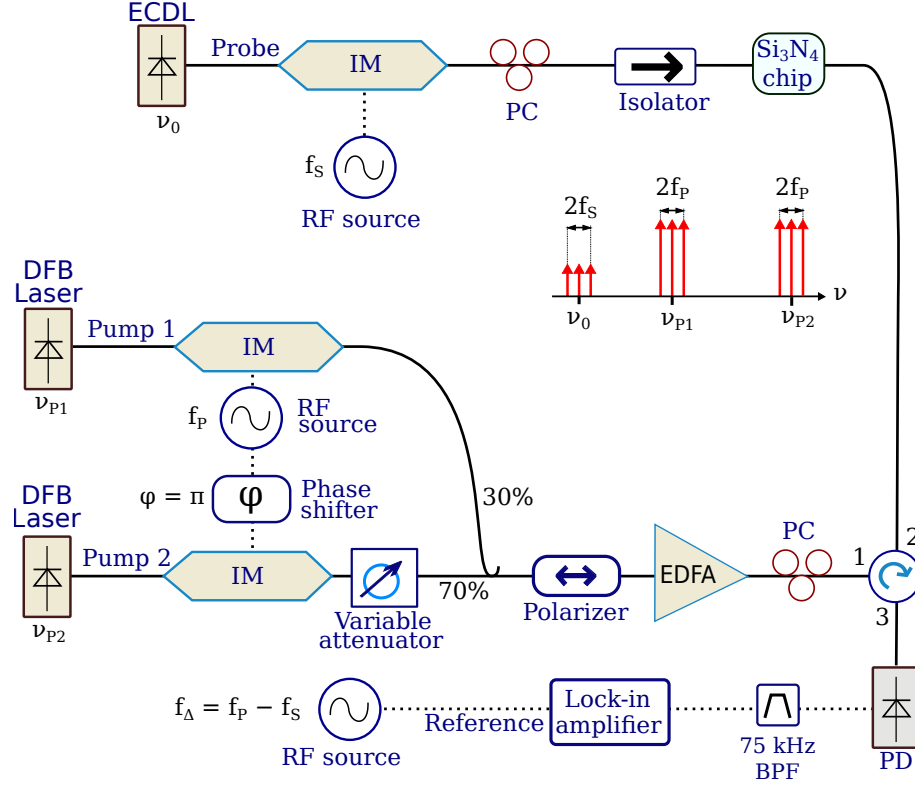


Figure S3: **Detailed experimental setup..** Precise intensity matching is realized by controlling a variable attenuator. Precise polarization matching is realized by letting the two pump beams pass through a polarizer. Note that the three RF sources generating the frequencies f_P , f_S and f_Δ are synchronized to a common time base. ECDL, external-cavity diode laser; DFB laser, distributed feedback laser; IM, intensity modulators; EDFA, erbium-doped fiber amplifier; PC, polarization controller; BPF, band-pass filter.

$$\frac{\partial E_s}{\partial z} + \frac{n_g}{c} \frac{\partial E_s}{\partial t} = \frac{1}{2} g_B P_P(z, t) E_s(z, t), \quad (14)$$

where c is the speed of light in vacuum, n_g is the group refractive index, g_B is the Brillouin gain and $P_P(z, t)$ is the power of the counter-propagating pump. Equation (14) assumes that the pump-probe frequency detuning is at the peak of the Brillouin gain and neglects the waveguide losses.

System response

We assume that both pump and probe modulation frequencies, f_P and f_S , are much smaller than $c/(n_g L)$ and that the difference of the frequencies, $|f_P - f_S|$, is much smaller than the Brillouin linewidth. These two assumptions are met in our experiments. Solving Eq. (14) in the small gain approximation using Eq. (13) for both pump evolution (assuming no pump depletion) and probe initial condition (at $z = 0$) leads to the following equation:

$$|A_{\text{det,peak}}| = 2 \cdot J_1(2\varsigma_P) \cdot J_1(2\varsigma_S) \cdot \rho_{\text{pd}} \cdot P_P \cdot P_S \cdot g_B \cdot L, \quad (15)$$

where the different symbols are described in Table (S1).

S5.2 Gain calculation

Equation (15) along with the mean value of the parameters presented in Table (S1) enable the determination of the Brillouin gain, $g_B = 6.87 \times 10^{-2} \text{ m}^{-1}\text{W}^{-1}$.

Symbol	Description	Value	Unit
$ A_{\text{det,peak}} $	Lock-in amplifier voltage at Si_3N_4 gain peak frequency	6.8	μV
P_S	Time-averaged probe power at detection	-12.51 ± 0.15	dBm
P_P	Time-averaged pump1 power inside the waveguide	20.8 ± 1	dBm
ρ_{pd}	Power-to-voltage conversion factor	6.14 ± 0.35	kV/W
L	Waveguide effective length, including inverse nanotapers	5 $^{+0}_{-0.3}$	mm
ς_P	Pump modulation depth	0.5142 ± 0.0071	
ς_S	Probe modulation depth	0.7197 ± 0.0011	

Table S1: Main parameters used for computation of the Brillouin gain from the system response.

S5.3 Error bar estimation

The uncertainty in the gain estimation comes from the imprecise knowledge of the parameters involved in Eq. (15). The uncertainties of the parameters are provided in Table (S1).

Explanation of the error bars: The uncertainty of P_S comes from the standard deviation of repeated measurements. The uncertainty of P_P comes from the uncertainty about the balance of the coupling loss on each side of the waveguide, that is estimated to be ± 1 dB. The uncertainty of ρ_{pd} comes from the standard deviation of repeated measurements. The uncertainty of L comes from the lack of knowledge about the nanotapers contribution to the total Brillouin gain, that is estimated to be $5^{+0}_{-0.3}$ mm. Finally, the uncertainty of the two modulation depths, ς , comes from the standard deviation of repeated measurements. Assuming Gaussian distributions and applying propagation of errors, the resulting uncertainty for the Brillouin gain, g_B , is $(8 \pm 1) \times 10^{-14} \text{ m/W}$ and g_B/A_{eff} is $(0.07 \pm 0.01) \text{ m}^{-1}\text{W}^{-1}$. Since the photoelastic constant is proportional to the square root of the Brillouin gain, propagation of errors gives a value of: $|p_{12}| = 0.047 \pm 0.004$. The additional error coming from the finite-element simulation as well as from the estimation of the acoustic Q-factor (obtained from Lorentzian fitting of the Brillouin gain), is assumed negligible.

S6 Threshold calculation

In order to estimate the corresponding SBS critical power (commonly referred as "SBS threshold" in the literature) in our Si_3N_4 waveguide, the presence of only one pump of power P_P and frequency ν_P is considered

in the waveguide. The power reflection coefficient R , due to Brillouin back-scattering is given by [12]:

$$R = Y e^{G/2} (I_0(G/2) - I_1(G/2)), \quad (16)$$

where I_m are the modified Bessel functions of the first kind of m -th order, $G = g_B \cdot P_P \cdot L$ is the unitless gain with L being the waveguide length. The parameter Y is defined as:

$$Y = \frac{1}{4}(\bar{n} + 1)g_B \cdot h\nu_P \cdot \Gamma \cdot L, \quad (17)$$

where h is the Planck constant, Γ is the Si_3N_4 acoustic damping rate and $\bar{n} = (e^{h\nu_B/kT} - 1)^{-1}$ is the mean number of phonons per acoustic mode (of frequency ν_B) at temperature T , k is the Boltzmann constant. The SBS threshold is conventionally defined as the required gain for $R(G_{\text{crit}}) = 0.1$. Therefore, the critical gain is estimated as $G_{\text{crit}} \approx 29$ at room temperature, and the SBS threshold is estimated as $P_{\text{crit}} \approx 87$ kW.

Bibliography

- [1] Herr, T. Solitons and dynamics of frequency comb formation in optical microresonators. Tech. Rep., EPFL (2013). URL <https://infoscience.epfl.ch/record/188349?ln=fr>.
- [2] Saleh, B. E. A. & Teich, M. C. *Fundamentals of Photonics; 2nd ed.* Wiley series in pure and applied optics (Wiley, New York, NY, 2007).
- [3] Stolen, R. H., Gordon, J. P., Tomlinson, W. & Haus, H. A. Raman response function of silica-core fibers. *Journal of the Optical Society of America B* **6**, 1159–1166 (1989). URL <https://www.osapublishing.org/josab/abstract.cfm?uri=josab-6-6-1159>.
- [4] Luke, K., Dutt, A., Poitras, C. B. & Lipson, M. Overcoming Si_3N_4 film stress limitations for high quality factor ring resonators. *Optics Express* **21**, 22829–22833 (2013). URL <http://www.opticsexpress.org/abstract.cfm?URI=oe-21-19-22829>.
- [5] Xuan, Y. *et al.* High-Q silicon nitride microresonators exhibiting low-power frequency comb initiation. *Optica* **3**, 1171–1180 (2016). URL <http://www.osapublishing.org/optica/abstract.cfm?URI=optica-3-11-1171>.
- [6] Liu, J. *et al.* Ultralow-power chip-based soliton microcombs for photonic integration. *Optica* **5**, 1347–1353 (2018). URL <http://www.osapublishing.org/optica/abstract.cfm?URI=optica-5-10-1347>.
- [7] Liu, J. *et al.* Double inverse nanotapers for efficient light coupling to integrated photonic devices. *Optics Letters* **43**, 3200–3203 (2018). URL <http://ol.osa.org/abstract.cfm?URI=ol-43-14-3200>.
- [8] Raja, A. S. *et al.* Packaged photonic chip-based soliton microcomb using an ultralow-noise laser. *arXiv* **1906.03194** (2019). URL <https://arxiv.org/abs/1906.03194>.
- [9] Pierson, H. O. *Handbook of chemical vapor deposition: principles, technology and applications*, chap. 10, 281 (William Andrew, 1999).
- [10] Qiu, W. *et al.* Stimulated Brillouin scattering in nanoscale silicon step-index waveguides: a general framework of selection rules and calculating SBS gain. *Optics Express* **21**, 31402–31419 (2013). URL <https://www.osapublishing.org/oe/abstract.cfm?uri=oe-21-25-31402>.
- [11] Boyd, R. W. *Nonlinear Optics*, 436–440 (Elsevier, 2003).
- [12] Boyd, R. W., Rzazewski, K. & Narum, P. Noise initiation of stimulated Brillouin scattering. *Physical Review A* **42**, 5514 (1990). URL <https://journals.aps.org/pr/a/abstract/10.1103/PhysRevA.42.5514>.